International Journal of Multiphase Flow 35 (2009) 1130–1137

Contents lists available at ScienceDirect

International Journal of Multiphase Flow

journal homepage: www.elsevier.com/locate/ijmulflow

Near-critical CO_2 liquid–vapor flow in a sub-microchannel. Part II: Flow regimes

Shi-Ming Li [1], Danesh K. Tafti *

Mechanical Engineering Department, Virginia Polytechnic Institute and State University, Blacksburg, VA 24061, United States

ARTICLE INFO

Article history:
Received 3 November 2008
Received in revised form 9 July 2009
Accepted 20 July 2009
Available online 23 July 2009

Keywords:
Liquid–vapor interfacial flow
Flow regime
Submicrochannel
Near critical CO_2

ABSTRACT

The mean-field free-energy LBM is used to investigate the liquid–vapor flow regimes in a two-dimensional 200 nm channel with near-critical CO_2 at temperature 25 °C and pressure 6.434 MPa as the working fluid. Flow regimes over vapor qualities ranging from $0.01 \leqslant x \leqslant 0.90$, Weber numbers $O(10^{-2}) \leqslant We \leqslant O(10^{3})$, and capillary numbers $O(10^{-2}) \leqslant Ca \leqslant O(10)$ are investigated. Three major types of flow regimes are encountered – dispersed flow, bubble/plug flow, and liquid strip flow, each of which encompasses variations of the basic flow regime. The three major flow regimes with all their variations can be further classified into two major categories – regular and irregular. Irregular flow regimes are characterized by a distorted interface, including distorted bubble/slug flow, intermittent strip flow, wavy strip flow, and wispy-strip flow. Flows in which the interface is ordered and symmetric such as bubble/plug and strip flows are classified as regular flow regimes. It is found that the transition from regular to irregular flow regimes occurs at Weber number between 500 and 1000, independent of the vapor quality. Although no experiments exist at the same conditions, comparison of the predicted transition between regular and irregular regimes shows the same qualitative trends as experiments found in the literature.
© 2009 Elsevier Ltd. All rights reserved.

1. Introduction

The natural refrigerant CO_2 has zero ozone depletion potential and significantly less global warming potential compared to other refrigerants, and thus is considered as the leading replacement refrigerant for mobile refrigeration/air-conditioning systems. In addition, CO_2 is non-toxic, non-flammable, and is abundant in nature. Its critical temperature of 30.98 °C (at a pressure of 7.377 MPa) provides supercritical and subcritical operating temperatures close to room and atmospheric temperatures. These properties make it quite attractive as a refrigerant in various applications.

The high operating pressure of the near critical CO_2, however, poses a major challenge in that its liquid–vapor two-phase flow properties may be very different from other fluids for which phase-change characteristics are better understood. For example, at a representative temperature of 25 °C, which is between the condenser and evaporator operating conditions for most vapor compression systems, CO_2 operates near the critical point at a reduced pressure, $p_r = 0.87$, and exhibits phase density ratios (n_l/n_v), viscosity ratio (μ_l/μ_v) of 2.9, and surface tension of 5.6×10^{-4} (N/m). At the same temperature, tetrafluoroethane (R134a) operates at $p_r = 0.16$, phase density ratio (n_l/n_v) of 37, and viscosity ratio of 16 with a surface tension of 8.1×10^{-3} (N/m), an order of magnitude larger. Because two-phase flow mechanisms are strongly dependent on the relative influence of inertial, viscous, gravitational and surface tension forces, the near-critical CO_2 liquid–vapor flow may yield drastically different flow characteristics from the more commonly investigated working fluids. For example, experimental work in the literature on flow regime maps is often performed with air–water systems, having a density ratio of 1000, a viscosity ratio of 46, and a surface tension of 7.2×10^{-2} (N/m), which are between one and two orders of magnitude larger than the near-critical CO_2 system.

From the engineering viewpoint it is important to characterize the two-phase system in order to predict friction and heat transfer characteristics. It is widely recognized that different flow regimes can yield substantially different characteristics of flow and heat transfer. Good literature reviews can be found for liquid–vapor flows with strong phase transitions, such as the review on boiling flow and heat transfer in microchannels reviewed by Kandlikar (2006) and the Yarin et al. (2008). In this paper our focus is on flow regimes and regime transitions under adiabatic conditions.

Most flow regime maps have been obtained by visualizing liquid–gas systems in macrochannels (D_h >6 mm, D_h is the channel hydraulic diameter) and minichannels (200 μm< D_h <6 mm), with much less work in microchannels (10 μm< D_h <200 μm). Serizawa et al. (2002), Kawaji and co-workers (Kawahara et al., 2002; Chung and Kawaji, 2004; Chung et al., 2004; Kawaji and Chung, 2004 and Kawahara et al., 2005), and Cubaud et al., (2006) are among the few researchers who have investigated flow regimes in microchannels. Serizawa et al., (2002) visualized air–water flow in circular tubes of

* Corresponding author. Tel.: +1 540 230 9975; fax: +1 540 231 9100.
E-mail addresses: smingli@revcor.com (S.-M. Li), dtafti@vt.edu (D.K. Tafti).
[1] Address: Revcor Fans and Blowers, 251 Edwards Ave, Carpentersville, IL 60110, United States.

0301-9322/$ - see front matter © 2009 Elsevier Ltd. All rights reserved.
doi:10.1016/j.ijmultiphaseflow.2009.07.007

20, 25 and 100 μm and for steam–water flow in a 50 μm circular tube. Kawaji and his co-workers, on the other hand, presented the flow maps for 50, 75, 100, 251, and 530 μm diameter circular channels, and one map for a square channel with D_h = 96 μm.

Among these studies all researchers have observed highly unsteady flow with multiple flow regimes appearing at the same location and under the same flow conditions. However, different groups observed very different flow regimes. Serizawa et al. (2002) recorded some flow regimes similar to those occurring in macrochannels, such as dispersed bubbly flow, slug flow, annular flow, wispy annular flow, and liquid droplet flow (see Brennen (2005) for macrochannels). Some of the flow regimes were close to those found in minichannels, such as rivulet flow (Barajast and Panton, 1993) and a very long, narrow Taylor bubble, up to ten times the channel diameter (Mishima and Hibiki, 1996). In addition, some flow regimes observed by Serizawa et al. (2002) had not been observed in larger channels, including *liquid-ring flow*, *liquid lump flow*, and *skewed barbecue shaped flow*. Kawaji and coworkers, on the other hand, categorized all their recorded flow regimes into slug flow but with different variations. They observed a *serpentine-like gas core flow* and *a ring-slug flow* which had not been observed previously in macro- and minichannels. Serizawa et al. (2002) and Cubaud et al. (2006) also studied the effect of wettabilities on flow regimes. Both groups found that different wettabilities affected the flow regimes in microchannels significantly. In addition, both observed that non-wetting walls generated more unsteady flow patterns than wetting walls, leading to non-symmetrical flow patterns and bubbles concentrated in the corners of the ducts.

When the channel size further decreases to sub-micron levels (100 nm < D_h < 10 μm), observation on flow regimes becomes more difficult and very few groups have explored this area, due to the limitation of conventional microscale flow measurement techniques. Tas et al. (2003) examined a liquid water plug in a rectangular channel with 10 μm wide and 100 nm high. They found that the water plug in the hydrophilic channel generated a significant pressure jump (as high as 17 ± 10 bar) due to capillary forces. Rossi et al. (2004) observed water liquid–vapor flow in a hydrophilic channel with contact angles between 5 and 20°. They captured the behavior of liquid menisci inside a 200–300 nm diameter circular carbon channel and showed that the interfaces (the meniscus) mainly appeared in asymmetrical shapes, and in particularly, the shapes were very irregular or complex. Kim et al. (2004) investigated liquid filling in submicron-carbon pipes. By plotting the filling length against time, they found a good fit with the well-known Washburn equation of capillary rise for long observation times (milliseconds). This result implied that the continuum assumption was still valid at this scale.

Using CO_2 as the working fluid, most previous studies have been conducted in macrochannels and minichannels and have focused on the friction and heat transfer characteristics (Thome and Ribatski, 2005; Yun and Kim, 2004a,b; Yun et al., 2005a,b; Park and Hrnjak, 2005 & 2007; Choi et al., 2007). There have been very few efforts to systematically observe and map the different flow regimes. The few groups which have investigated this aspect differ in their observations due to different flow conditions, channel sizes, cross sections, and other reported factors.

The objective of this paper is to investigate numerically the flow regimes which are encountered in a sub-microchannel with near-critical CO_2 as the working fluid. In the current paper, we limit our discussions to adiabatic liquid-vapor flows including condensation and evaporation. To the best of the authors' knowledge, there are no numerical simulations which have tried to resolve the flow regime maps, mostly because of the complex interplay between different competing forces of inertia, viscosity, capillarity, thermodynamic phase properties, and surface wettability. A two-dimensional smooth channel of height 200 nm is considered with CO_2 at 25 °C and a pressure of 6.434 MPa at the different vapor fractions ranging from 0.01 to 0.9. A partially wetting wall is considered with a static contact angle of 45°. The numerical tool in the current study is the mean-field free-energy LBM, developed in Li and Tafti (2009). Careful consideration is given in the current paper to scaling the LBM to the actual physical conditions to maintain thermodynamic consistency as well as the correct interfacial surface tension and hydrodynamic properties of the two fluid phases.

2. Scaling considerations

In order to include the specific physical and thermodynamic phase properties of CO_2 into the simulations, the LBM system is scaled explicitly to the physical system. The scaling is performed to satisfy the following physical conditions: (1) The resulting surface tension in the calculation is the same as the actual physical value. (2) The fluid viscosities of both liquid and vapor are the same as the actual physical values. (3) The thermodynamic properties are the same as the actual physical values at equilibrium, including: (a) The bulk phase pressure in equilibrium is constant for the two phases with a planar interface and is equal to the actual saturation pressure at the corresponding temperature. (b) The fluid densities of the two bulk phases at equilibrium are equal to the actual physical liquid and vapor densities at equilibrium. (c) The chemical potentials of the two bulk phases are constant and equal at equilibrium. These conditions ensure the physical and thermodynamic consistency of the model. Table 1 identifies the physical quantities together with the scaled LBM quantities (see Supplementary material in the online version of this article for details), where Δr is the lattice length, Δt is the lattice time unit and Δm is the particle mass, a and b are the van der Waals constants for CO_2, K is the constant representing the effective fluid–fluid attraction potential, ω is the LBM relaxation factor, and T_r is the relative temperature.

3. Results

3.1. Simulation geometry and conditions

The simulation geometry consists of a two-dimensional channel of height 200 nm and length 1000 nm. CO_2 at a pressure of 6.434 Mpa and a temperature of 298 K is simulated at different vapor qualities, x. Applying the scaling choice of Δr = 1.0 nm listed in Table 1, the channel dimension in LBM lattice units is 200 lattice units high and 1000 lattice units long.

Table 1
LBM scaling results of CO_2 at 25 °C.

Variables		LBM	Physical
i1	T_c	0.1	304 (K)
i2	Δr	1	0.001 μm
i3	b	4/21	0.0007246 m^3/kg
	T_r	0.9796187	0.979618672
1	T	0.0979619	298 (K)
2	a	0.0676095	120.45 m^5/(kg. s^2)
3	Δm	1	2.628847E–25 kg
4	Δt	1	1.4612613E–12 s
5	P	0.0522603	6.434 Mpa
6	n_L	2.7113406	713 kg/m^3
7	n_V	0.9163713	241 kg/m^3
8	ν_L	1.184E−01	8.105E−8 m^2/s
9	ν_V	1.208E−01	8.264E−8 m^2/s
10	γ	0.00454	5.584E−4 N/m
r1	K	0.06000	NA
r2	ω_L	1.169E+00	NA
r3	ω_V	1.160E+00	NA

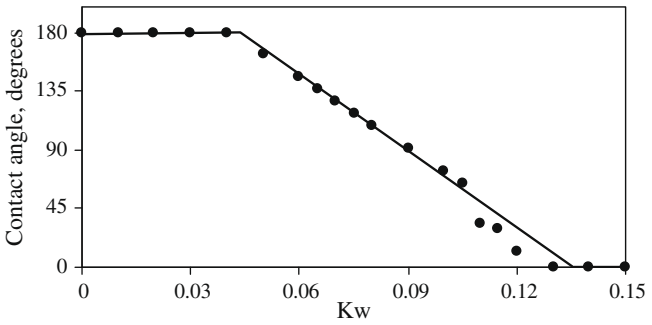

Fig. 1. CO_2 liquid droplet on walls of different wettabilities.

To simulate a specific wettability of the channel wall, we first performed a series of simulations of an isolated CO_2 droplet on a solid wall with different values of K_w, the fluid–wall interaction force coefficient (Eq. (22) in Li and Tafti, 2009). Different liquid and vapor CO_2 viscosities were simulated, according to Table 1, by using different relaxation factors. Once steady state was achieved, where the spurious residual velocities in the domain were of $O(10^{-7}$–$10^{-8})$, the contact angle of the droplet was deduced from the contour line at the average fluid density. The correlation between K_w and contact angle obtained from multiple simulations is shown in Fig. 1, where the points are the simulation results and the solid line is a piecewise best linear fit to the calculations. For CO_2 liquid–vapor flow in the 200 nm microchannel, we studied the partial wetting condition with the equilibrium contact angle of 45°, which is equivalent to $K_w = 0.11$ based on Fig. 1.

Periodic boundary conditions were applied in the axial flow direction of the channel under the assumption of spatially fully-developed flow. For liquid–vapor two phase flow at the sub-micron scale, very little is known about slip flow characteristics due to non-continuum effects (Barber and Emerson, 2006; Xu and Li, 2007). However, using kinetic theory, the Knudsen number ($Kn = \lambda/H$) for CO_2 vapor under the present conditions is of $O(10^{-3})$ (λ is the mean free path and H is the height of the channel), indicating the general validity of the continuum assumption. Hence no-slip boundary conditions are applied at the solid surfaces of the channel in the current study.

The initial conditions are specified with alternating liquid and vapor plugs distributed along the length of the channel, as shown in Fig. 2, for each simulated vapor fraction or quality x. In the figure, L_L and L_V represent the lengths of each liquid and vapor column, respectively, and L_c the length of the channel. A fixed vapor quality is obtained in the channel with the following constraints:

$$(L_L + L_V)N_p = L_c \ (N_p \text{ is an integer}) \tag{1}$$

$$\frac{L_V}{L_V + L_L} = \frac{x n_L}{n_V(1-x) + x n_L} \tag{2}$$

Table 2 shows the liquid and vapor length combinations used for 10 different x with a fixed $N_p = 5$ in the simulations presented in this paper.

Table 2
L_L and L_V at each x for CO_2 at 25 °C.

Condition	x	$L_V/(L_V + L_L)$	$L_L/(L_V + L_L)$	L_V	L_L
1	0.01	0.032	0.968	6	194
2	0.03	0.091	0.909	18	182
3	0.05	0.146	0.854	29	171
4	0.1	0.265	0.735	53	147
5	0.25	0.519	0.481	104	96
6	0.5	0.764	0.236	153	47
7	0.6	0.829	0.171	166	34
8	0.7	0.883	0.117	177	23
9	0.8	0.928	0.072	186	14
10	0.9	0.967	0.033	193	7

An initial parabolic velocity field is specified in the channel cross-section. To provide the motive force, a constant body force $\mathbf{F}_o(\mathbf{x}) = f\mathbf{i}_x$ (equivalent to the pressure gradient) is applied in the axial direction, where f is a constant. Different Reynolds numbers or mass flow rates are realized through different values of f. For each vapor quality x, we simulate four different body forces 1.662×10^6, 3.324×10^5, 3.324×10^4, and 3.324×10^3 MPa/m, for most of the cases. For the three cases at $x = 0.60$, 0.80, and 0.90, the maximum force level is reduced to 9.972×10^5 MPa/m to maintain numerical stability.

For each simulated case, the flow condition is characterized by the Reynolds number Re, capillary number Ca, and Weber number We at its stationary state, which are defined as

$$Ca = \mu_{AV}V/\gamma, \quad \mathrm{Re} = 2H_C V n_{AV}/\mu_{AV}, \quad We = \mathrm{Re}\cdot Ca = 2H_C n_{AV}V^2/\gamma,$$

where the subscript AV represents the average value of the related parameter; H_C is the channel height; and V is the channel flow average velocity, which is obtained as the time-averaged mass flow rate divided by the average fluid density and channel cross-sectional area.

To compare our results with those in the literature, we also compute the gas or vapor superficial velocity, J_G and the liquid superficial velocity J_L. Their definitions are:

$$J_G = \dot{m}_G/n_G H_C = x\dot{m}/\rho_G H_C, \quad J_L = \dot{m}_L/n_L H_C = (1-x)\dot{m}/\rho_L H_C,$$

where $\dot{m}$ is the mass flow rate per unit channel width and the subscripts G and L represents vapor and liquid, respectively (Here using the subscript G rather than V is to be consistent with the chart cited from the literature latter in this paper). The Reynolds numbers based on the superficial velocities are accordingly given as follows:

$$\mathrm{Re}_L = 2H_C J_L n_L/\mu_L; \quad \mathrm{Re}_G = 2H_C J_G V n_V/\mu_V.$$

3.2. Stationary flow regimes and transition boundary maps

Different flow conditions generate different stationary flow regimes after going through a series of transient patterns (Li, 2007). Typically each calculation is run for between 200,000 and 800,000 time steps before a stationary flow regime is obtained

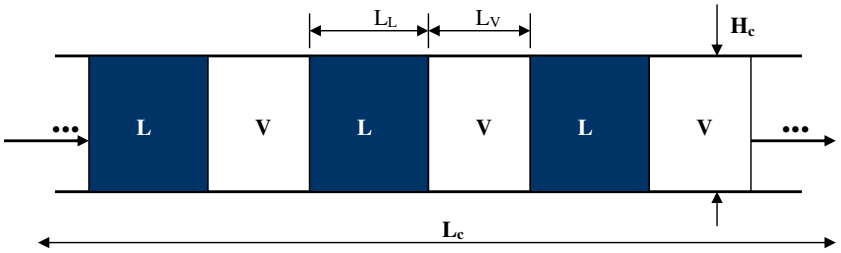

Fig. 2. A schematic of simulation setup for 2D channel flows, L_c and H_c are channel length and height, respectively; L_L and L_V represents liquid length and vapor length, respectively.

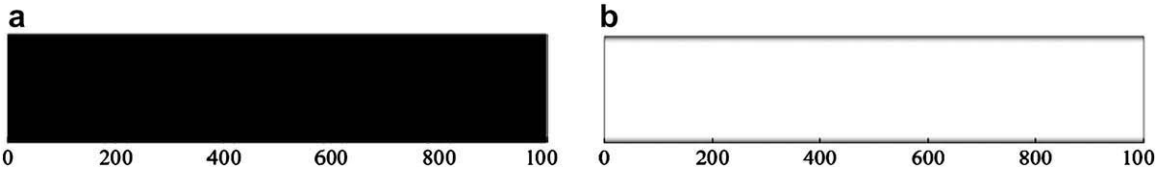

Fig. 3. Dispersed types: (a) vapor dispersed flow, $x = 0.01$, $We = 4810$ and (b) liquid dispersed flow, $x = 0.90$, $We = 415.32$.

and ascertained. This amounts to about two weeks of computing time on a single SGI-Altix CPU. The forty different flow conditions simulated, with 10 different vapor qualities x and four levels of driving forces $\mathbf{F}_o(\mathbf{x}) = f\mathbf{i}_\mathbf{x}$ at each x cover the Weber number range over five orders of magnitude, from $O(10^{-2})$ to $O(10^3)$. The competition between capillary, inertia, viscous forces, and the surface wettability gives rise to a series of complex flow regimes. Under the forty flow conditions, three major types of flow regimes occur: dispersed types, bubble types, and liquid strip types, each of which encompasses variations of the basic flow regime, as will be discussed in detail in this section.

When vapor quality is at one of the two extremities, too small or too large, the minor phase in the fluid is dispersed in the major phase and the fluid density appears uniformly distributed as if the flow was a single phase flow, as shown in Fig. 3. At very low vapor quality with all four cases at $x = 0.01$ and some cases at $x = 0.03$, the small vapor composition in the fluid is dispersed in the continuous liquid phase and a *vapor dispersed flow* occurs, as shown in Fig. 3(a). In the *vapor dispersed flow,* the fluid density appears uniform almost everywhere in the channel and its magnitude in the current study is around 99% of the saturated liquid density. The exception is the density of the very thin layer of fluid on the walls, which is around 94% of the fluid density in the core area. This is the typical fluid characteristic of a partial-wetting wall. At the other extremity of a very high vapor quality at $x = 0.9$, on the other hand, a *liquid dispersed flow* occurs. Under this condition, part of the liquid in the flow forms a very thin liquid film on the channel walls, as shown in Fig. 3(b). The other part of the liquid is dispersed uniformly in the vapor phase. Similar to the vapor dispersed flow, the fluid density in the liquid dispersed flow appears uniform in the main area of the channel and the fluid density in the core area is slightly larger than the saturated vapor density. In the literature, this flow pattern is sometimes called *mist flow*.

When vapor quality increases from the lowest extremity to a threshold, it leads to the formation of vapor bubble. The threshold to form a concentrated vapor bubble depends on both vapor quality and inertia, which is expressed by the non-dimensional parameters *Re* and *We*. At $x = 0.03$, a bubble forms only at the maximum inertia level or the maximum *Re* and *We*, indicating that large flow inertia may aid the coalescence of dispersed vapor to form a bubble at the low vapor quality. With an increase in vapor quality to $x = 0.05$, bubbles form at all four levels of *Re* or *We*, indicating that the vapor quality for bubble formation becomes independent of the other flow condition at the higher vapor quality.

In the literature, a bubble equal to or larger than the channel characteristic length is commonly referred to as a plug. Our simulation results show that a plug starts to form at $x = 0.05$. Fig. 4 shows the typical bubble/plug flows appearing in the simulations.

At low Weber numbers, the relatively large capillary forces keep the bubble/plug in symmetry, yielding the *symmetric bubble/plug* flow. When Weber number increases to $O(10^3)$, the bubble/plug becomes distorted *(distorted bubble/plug)* under the effect of the large inertia. On the other hand, at the lower vapor quality ($x = 0.03$–0.1), the flow pattern appears in the form of *single bubble/plug*. When the vapor quality increases to $x = 0.25$–0.50, the initial bubble pattern remains unchanged since the liquid bridge between two consecutive vapor bubbles is thick enough to keep the plug train from coalescing with each other. Consequently, the *bubble trains or plug trains* form at small *We* at $x = 0.25$ and 0.50. Among the plug flow patterns, two types of plug flows were encountered. One was the *submerged plug* at $We \geqslant O(100)$, in which a liquid layer existed between the plug and the channel

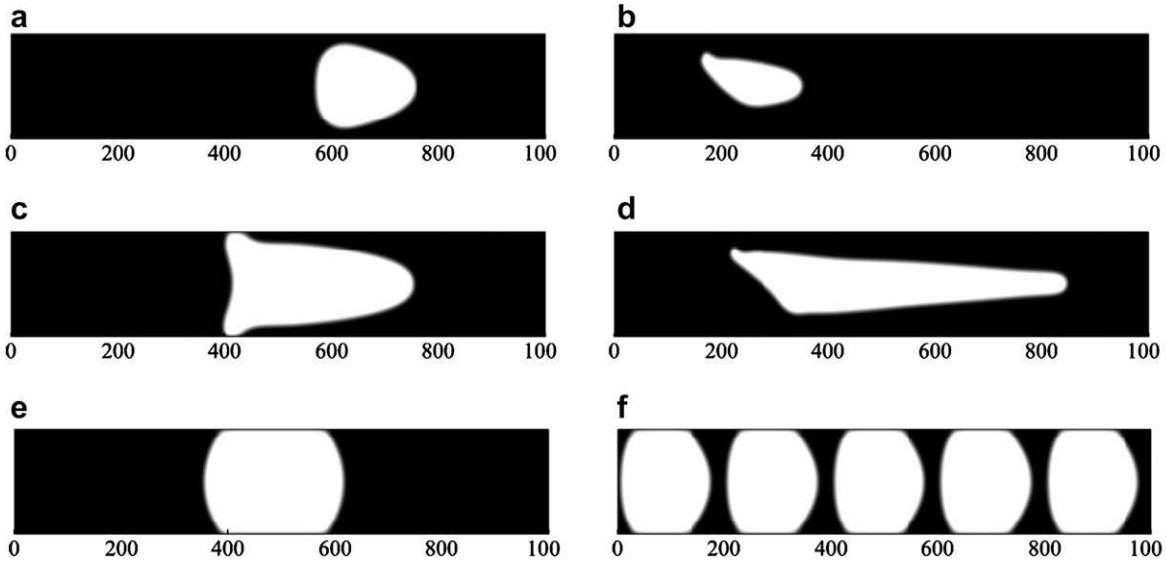

Fig. 4. Bubble types: (a) single, symmetric, submerged bubble flow, $x = 0.05$ and $We = 185.1$; (b) single, distorted bubble flow, $x = 0.03$, $We = 4567$; (c) single, symmetric, submerged plug flow, $x = 0.10$, $We = 182$; (d) single, distorted plug flow, $x = 0.10$, $We = 4005$; (e) single, symmetric, non-wetting plug flow, $x = 0.10$, $We = 0.0082$ and (f) symmetric, non-wetting plug train flow, $x = 0.50$, $We = 3.02$.

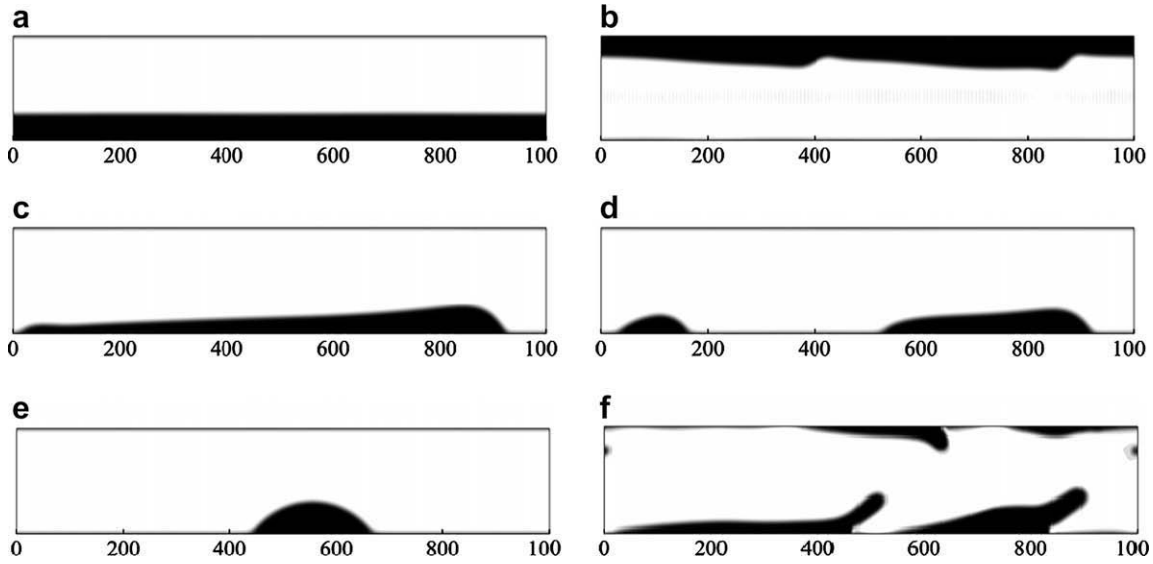

Fig. 5. Liquid strip types: (a) stratified-strip flow, $x = 0.50$, $We = 205.5$; (b) wavy-stratified or wavy-strip flow, $x = 0.50$, $We = 4831$; (c) intermittent strip flow, $x = 0.70$, $We = 262.41$; (d) intermittent strip flow, $x = 0.8$, $We = 313.45$; (e) liquid lump flow, $x = 0.90$, $We = 0.0426$ and (f) wispy-strip flow, $x = 0.70$, $We = 2891$.

wall. The other was the *non-wetting plug* at $We \leqslant O(1)$, which completely adhered to the wall with a dry patch on the surface of the wall. The non-wetting plug is peculiar to partial-wetting and non-wetting conditions.

When *We* numbers becomes of $O(100)$ or larger at the vapor quality of $x = 0.25$ and 0.50, the bubbles of the plug train merge with each other and form a continuous vapor core in the channel with the liquid layer attached on the wall. This is a *liquid strip flow* in the 2-D channel geometry, which is similar to an annular flow of a circular pipe in the literature. In the current study, only asymmetrical strip flow pattern appears due to the partial-wetting properties of the channel walls. With a usual symmetric annular-like strip pattern, there were two layers of liquid, each on either side of the channel wall. The "drying layer" between the liquid layer and the partially wetting walls would add an additional liquid–vapor interface area to the fluid system, making it more unstable than one layer of liquid on one side of the wall. Hence the symmetric strip flow would be destabilized to eventually form an asymmetric stratified strip pattern at the current partial wetting condition or to either *a stratified* or *wavy-stratified pattern*, as shown Fig. 5. The difference between a stratified strip and wavy-stratified strip is that the latter develops a wavy interface due to the larger inertia effects at $We \sim O(1000)$.

As the vapor quality increases to $x = 0.70$ and higher, there is not enough liquid to form a continuous liquid layer at the walls, and an *intermittent strip flow* occurs as depicted in Fig. 5(c) and (d). The intermittent strip flow follows the form of a highly sheared liquid droplet and has a non-uniform thickness with advancing and receding contact angles as it is dragged along the channel wall driven by the core vapor flow. The intermittent strip flow occurs at medium *We* of $O(100)$. At lower Weber numbers and higher vapor quality $x > 0.70$, the small amount of liquid forms a droplet on the wall due to the relative large capillarity. This flow pattern is depicted in Fig. 5(e) and is referred to as *liquid lump flow* in the literature.

At $x > 0.7$ and at the highest Weber number $We \sim O(10^3)$, the large shear between the vapor core and the slower moving intermittent liquid layer near the wall tears off strips of liquid from the wall. Under such conditions, one end of the liquid strip slips on the wall and the other end is pulled by the core vapor flow, as shown in Fig. 5(f). Eventually, the strip of liquid pinches off from the wall or part of the strip is entrained into the core of the flow, forming streaks or wisps of liquid, which is analogous to wispy-annular flow in a circular pipe. The wisps of liquid in the core of the channel evaporate and then deposit/condense back on the walls of the channel to form new strips of liquid. We call this type of strip flow as *wispy-strip flow*, due to its similarity to the wispy-annular flow in a circular tube. It is noted that both the wispy-strip flow and wavy-strip flow occur in the same range of *We*. The difference between the two is that a wispy-strip flow appears at higher vapor quality.

Table 3
Summary of flow regimes, for CO_2 at 25 °C.

Dispersed types	Liquid dispersed flow Vapor dispersed/mist flow	*Note 1*: Dispersed flow occurs at the extreme vapor qualities, no variation of the flow regimes with *Ca*, *Re* and *We*;	
Bubble types	Bubbly flow	Symmetric bubbly flow Distorted bubbly flow	
	Plug flow	Symmetric plug flow	Single plug Plug train
		Distorted plug flow	
Strip Types	Stratified strip flow Wavy-stratified strip flow Intermittent strip flow	*Note 2*: Bubble flow occurs at low vapor quality	
	Liquid lump strip flow	*Note 3*: Liquid strip flow occurs at medium to high vapor quality, over the full range of *We*.	
	Wispy strip flow		

Table 4
Regular and irregular flow regimes, CO_2 at 25 °C.

Regular flow	Symmetric bubbly/plug flow
	Bubbly/plug train flow
	Stratified strip flow
	Liquid lump strip flow
Irregular flow	Distorted bubbly/plug flow
	Intermittent strip flow
	Wavy-stratified strip flow
	Wispy-strip flow

Table 5
L_L and L_V at $x = 0.25$ and 0.50 for different initial conditions.

x	$L_V/(L_V + L_L)$	$L_L/(L_V + L_L)$	Simulation	L_V	L_L
0.25	0.519	0.481	1	13	12
			2	26	24
			3	52	48
			4	*104*	*96*
0.50	0.764	0.236	1	38	12
			2	76	24
			3	*153*	*47*
			4	230	72
			5	306	94

From the above discussions, it is clear that the flow regimes are largely dependent on vapor quality and Weber number. Table 3 summarizes the flow regimes. With the variation of the vapor quality and Weber number, it is seen that the interfaces, in fact, either retain a regular shape or become distorted and irregular. Therefore, we further classify the flow regimes into two broad categories of *regular* and *irregular* flows. Table 4 summarizes the classification of the different flow regimes encountered.

The flow regime map shown in Fig. 6 further summarizes most of the simulated results described above, except the dispersed flows at the two extreme vapor qualities. In the Figure, the shadowed boundaries give a range over which flow regime transitions occur. The figure shows that the transition boundary between regular interface flow regimes and irregular interface regimes depends mainly on *We* number alone and exists near $We = 500$–1000. The transition boundary between the bubble and strip regimes, on the other hand, depends mainly on the vapor quality. When $We < 10$, the transition occurs between $x = 0.5$ and 0.6. When $We > 10$, the transition occurs between $x = 0.10$ and 0.20.

3.3. Effect of initial conditions

To examine the effect of initial flow conditions on the stationary flow regimes, we use several different initial fluid density patterns to perform a number of additional simulations for the vapor qualities of $x = 0.25$ and 0.50 (Table 5). The different initial density patterns are simulated through changing the relative lengths of liquid L_L over vapor columns L_V, based on Eqs. (1) and (2). For each initial flow pattern, the same four levels of body forces, as described earlier, are simulated. These additional results show that the final stationary flow regimes are not dependent on the initial conditions when the flow inertia is large enough or when the initial liquid–vapor interface is thin enough such that the initial flow pattern is broken up as the flow evolves toward the stationary state. Only when *We* is of $O(1)$ or below and the initial liquid–vapor interface is thick enough, as shown in the shaded area in Fig. 6, the stationary flow pattern remains the same or similar to that given by the initial flow pattern leading to the *bubble/plug* type flow.

3.4. Comparisons with other flow regime maps

We attempt to compare the flow regimes obtained for the near-critical CO_2 in the 200 nm channel with past work in the literature. This is a difficult task since there are no direct experimental studies at these conditions and all flow regime maps have been constructed in much bigger channels mostly using air–water systems. However, it is important to note that CO_2 near the critical point has viscosity much lower than an air–water system ($\sim 8 \times 10^{-8}$ m^2/s for CO_2 versus $\sim 1 \times 10^{-5}$, $\sim 1 \times 10^{-6}$ m^2/s for air–water) and surface tension which is also much lower ($\sim 5 \times 10^{-4}$ N/m for CO_2 versus $\sim 7 \times 10^{-2}$ N/m for air–water). Hence the flow regime maps would still have some equivalency in terms of Reynolds numbers and Capillary numbers when plotted against superficial liquid–vapor velocities in which the difference in length scale is partially compensated by the differences in viscosity and surface tension. Hence some qualitative similarity to other studies is expected.

Fig. 7 is the currently obtained flow regime map but plotted against liquid and vapor superficial velocities. In the figure, the

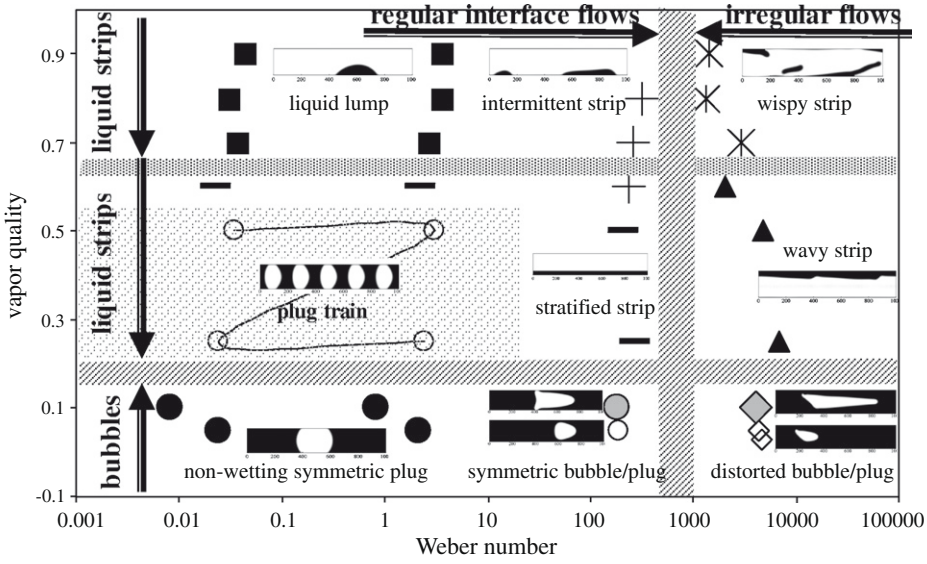

Fig. 6. Liquid–vapor flow regime map of a microchannel, CO_2, 25 °C. The shadowed bars represent the flow regime transition boundaries.

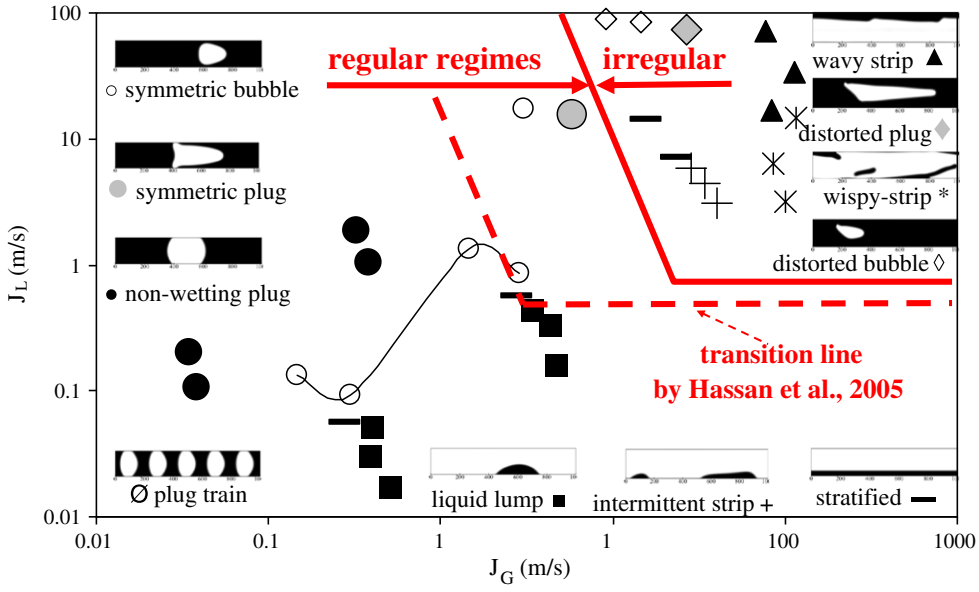

Fig. 7. 25 °C CO_2 liquid–vapor flow regime map of a microchannel. The thick solid line is the flow regime transient line between regular interface regimes and irregular interface regimes. The dashed line is the transient boundary deduced from the "universal flow map" by Hassan et al. (2005).

thick solid line is the flow regime transition line between regular interface regimes and irregular interface regimes. It is noticed that the transition boundary can be expressed as two connected straight lines in Fig. 7, rather than one thick straight line in Fig. 6.

Hassan et al. (2005) studied flow regime maps in minichannels and, based on their results, categorized the flow regimes into four groups: bubbly, intermittent (plug flow, plug-annular flow), churn, and annular. Based on their categorization, they incorporated the experimental data existing in the literature into their observations and proposed two "universal flow regime maps" for horizontal tubes with diameters ranging from 1 mm to 0.1 mm, and vertical minichannels with diameters ranging from 1 mm to 0.5 mm, respectively. They found that the universal flow regime maps gave a good approximation of the regime transitions for all studies made for minichannels. Based on the universal flow regime map for vertical tubes, we have deduced the boundary between regular and irregular interface flow regimes and plotted this flow regime boundary in Fig. 7, as displayed by the thick dashed lines. The figure shows that both, the present study and that by Hassan et al. have the transition boundaries consisting of two straight lines with one being horizontal. While there is better agreement of the transition boundary in the liquid superficial velocity J_L with our simulations, for the same J_L the present results indicate that a larger gas superficial velocity J_G can be sustained before the liquid–vapor interface becomes irregular. In spite of the expected differences between the two, there is good qualitative agreement.

We also compare our results to the work done by Serizawa et al. (2002) in 20 μm channel which is the smallest channel size having a complete flow regime map published in the literature using a air–water system. Based on our current flow regime map plotted against the liquid and vapor superficial velocities, as shown in Fig. 7, we find that the flow regime transition boundary between the various kinds of bubble flows and the liquid strip flows can be approximated by a straight line (not displayed directly in Fig. 7 to avoid possible confusion) while the same boundary is expressed by a few connected perpendicular straight lines in Fig. 6. We plot this boundary line in the flow map derived by Serizawa et al. (2002), as shown in Fig. 8. In the figure, the solid line is deduced by the current authors based on the results presented in the same figure by Serizawa et al. (2002). It is shown that the

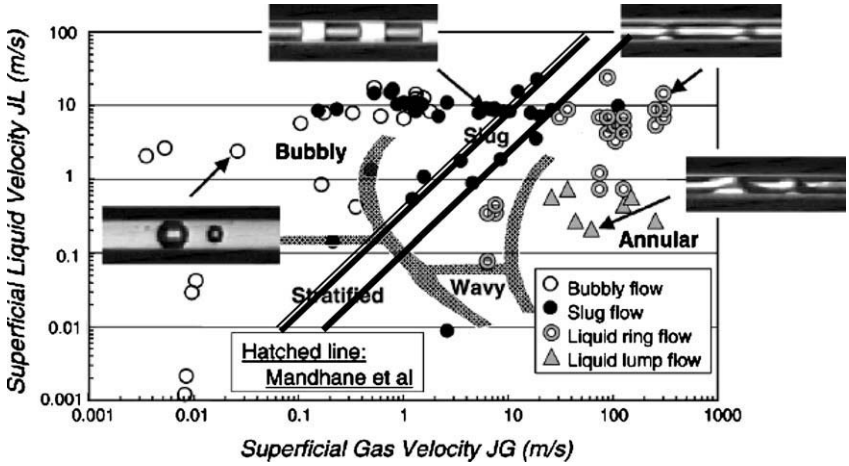

Fig. 8. Flow pattern map for air–water in a 20 μm diameter silica channel by Serizawa et al. (2002). The thick solid line is the flow regime transition boundary separating the bubble flow regimes from the strip flow regimes based on Serizawa, Feng, and Kawara. Double lines: the flow regime transition boundary derived from current simulations.

transition boundary of our results and the experimental results by Serizawa et al. are close to each other showing good qualitative agreement.

4. Summary and conclusions

The mean-field free-energy D2Q9 LBM is used to study near-critical CO_2 flow regimes at 25 °C in a 200 nm high sub-microchannel. The simulated wettability of the channel wall produces an equilibrium contact angle of 45°. Ten different vapor qualities are studied, from 0.01 to 0.90. For each vapor quality, Weber numbers that vary over five orders of magnitude, from $O(10^{-2})$ to $O(10^{3})$ are investigated.

Under the forty flow conditions, three major types of flow regimes occur – dispersed flow, bubble flow, and liquid strip flow. The dispersed flow includes vapor dispersed flow and liquid dispersed flow, and occurs at very low and very high vapor quality, respectively. When vapor quality increases beyond a threshold, there is enough vapor in the channel to form a vapor bubble. The threshold to form a vapor bubble depends on both vapor quality and Weber number. The bubble/plug flow includes symmetric and distorted, submerged and non-wetting, and single and train types. The transition boundary between the bubble and strip regimes depends mainly on vapor quality. When Weber number is less than ten, the transition occurs between vapor quality of 0.5 and 0.6. When Weber number is greater than ten, the transition occurs around vapor qualities of 0.10–0.20. At high Weber numbers when inertia is large enough to destroy the initial alternating liquid–vapor flow pattern, the transition boundary between the bubble and strip regimes depends only on vapor quality and exists between 0.10 and 0.20. The liquid strip flow includes stratified strip flow, wavy-stratified strip, intermittent strip flow, liquid lump flow, and wispy-strip flow.

The flow regimes are further classified into two major categories – regular and irregular. Irregular flow regimes are characterized by a distorted interface, including distorted bubble/slug flow, intermittent strip flow, wavy strip flow, wispy-strip flow. Flows in which the interface is ordered and symmetric such as bubble/plug and strip flow are regular flow regimes. With this definition, the results show that the transition from the regular to irregular flow regimes occurs at Weber number between 500 and 1000, independent of the vapor quality.

The flow maps and transition boundaries are represented in two different forms. One is the liquid versus vapor superficial velocity mapping and the other using the vapor quality and Weber number. The flow maps are compared with both the experimental "universal flow regime map" by Hassan et al. (2005) and the flow map for microchannels given by Serizawa et al. (2002). In spite of substantial differences between the experimental conditions and the simulations, the good qualitative agreement shows that the current simulations capture the basic and important flow mechanisms for the flow regime transition from bubble flow to strip flow and from regular flow regimes to irregular flow regimes.

To the best of the authors' knowledge, these are the first numerical simulations which have resolved the flow regime map resulting from a complex interplay between different competing forces of inertia, viscosity, capillarity, thermodynamic properties, and surface wettability. In addition, this is the first flow map obtained for submicrochannel flows, either experimental or otherwise. It is also the first adiabatic flow map for a near-critical CO_2 flow which has important practical applications.

Appendix A. Supplementary data

Supplementary data associated with this article can be found, in the online version, at doi:10.1016/j.ijmultiphaseflow.2009.07.007.

References

Barajas, A.M., Panton, R.L., 1993. The effects of contact angle on two-phase flow regimes in capillary flow. Int. J. Multiphase Flow 19, 337–346.

Barber, R.W., Emerson, D.R., 2006. Challenges in modeling gas-phase flow in microchannels: from slip to transition. Heat Transfer Eng. 27, 3–12.

Brennen, C.E., 2005. Fundamentals of Multiphase Flow. Cambridge University Press. p. 133.

Choi, K.-I., Pamitrana, A.S., Oh, J.-T., 2007. Two-phase flow heat transfer of CO_2 vaporization in smooth horizontal minichannels. Int. J. Refrigeration 30, 767–777.

Chung, P.M.-Y., Kawaji, M., 2004. The effect of channel diameter on adiabatic two-phase flow characteristics in microchannels. Int. J. Multiphase Flow 30, 735–761.

Chung, P.M.-Y., Kawaji, M., Kawahara, A., Shibata, Y., 2004. Two-phase flow through square and circular microchannels – effect of channel geometry. ASME J. Fluids Eng. 126, 546–552.

Cubaud, T., Ulmanella, U., Ho, C.-M., 2006. Two-phase flow in microchannels with surface modifications. Fluid Dyn. Res. 38, 772–786.

Hassan, I., Vaillancourt, M., Pehlivan, K., 2005. Two-phase flow regime transitions in microchannels: a comparative experimental study. Microscale Thermophys. Eng. 9, 165–182.

Kandlikar, S.G., 2006. Flow boiling in minichannels and microchannels. In: Garimella, S., Li, D., Colin, S., King, M.R. (Eds.), Heat Transfer and Fluid Flow in Minichannels and Microchannels. Elsevier, Boston and New York.

Kawahara, A., Chung, P.M.Y., Kawaji, M., 2002. Investigation of two-phase flow pattern, void fraction and pressure drop in a microchannel. Int. J. Multiphase Flow 28, 1411–1435.

Kawahara, A., Sadatomi, A., Okayama, K., Kawaji, M., Chung, P.M.-Y., 2005. Effects of channel diameter and liquid properties on void fraction in adiabatic two-phase flow through microchannels. Heat Transfer Eng. 26 (3), 13–19.

Kawaji, M., Chung, P.M.-Y., 2004. Adiabatic gas–liquid flow in microchannels. Microscale Thermophys. Eng. 8, 239–257.

Kim, B.M., Sinha, S., Bau, H.H., 2004. Optical microscope study of liquid transport in carbon nanotubes. Nano Lett. 4, 2203–2208.

Li, S.-M., 2007. Mean-field free-energy lattice Boltzmann method for liquid–vapor interfacial flows, Ph.D. thesis. Virginia Polytechnic Institute and State University.

Li, S.-M., Tafti, D.K., 2009. Near-critical CO2 liquid–vapor flow in a sub-microchannel. Part I: mean-field free-energy D2Q9 lattice Boltzmann method. Int. J. Multiphase Flow 35, 725–737.

Mishima, K., Hibiki, T., 1996. Some characteristics of air–water two-phase flow in small diameter vertical tubes. Int. J. Multiphase Flow 22, 703–712.

Park, C.Y., Hrnjak, P.S., 2005. Flow boiling heat transfer of CO_2 at low temperatures in a horizontal smooth tube. ASME Trans. J. Heat Transfer 127, 1035–1312.

Park, C.Y., Hrnjak, P.S., 2007. CO_2 and R410A flow boiling heat transfer, pressure drop, and flow pattern at low temperatures in a horizontal smooth tube. Int. J. Refrig. 30, 166–178.

Rossi, M.P., Ye, H., Gogotsi, Y., Babu, S., Ndungu, P., Bradley, J.-C., 2004. Environmental scanning electron microscopy study of water in carbon nanopipes. Nano Lett. 4, 989–993.

Serizawa, A., Feng, Z.P., Kawara, Z., 2002. Two-phase flow in microchannels. Exp. Therm. Fluid Sci. 26, 703–714.

Tas, N.R., Mela, P., Kramer, P., Berenschot, J.W., van den Berg, A., 2003. Capillarity induced negative pressure of water plugs in nanochannels. Nano Lett. 3, 1537–1540.

Thome, J.R., Ribatski, G., 2005. State-of-the-art of two-phase flow and flow boiling heat transfer and pressure drop of CO_2 in macro- and micro-channels. Int. J. Refrig. 28, 1149–1168.

Xu, J., Li, Y., 2007. Boundary conditions at the solid–liquid surface over the multiscale channel size from nanometer to micron. Int. J. Heat Mass Transfer 50, 2571–2581.

Yarin, L.P., Moysak, A., Hetsroni, G., 2008. Fluid Flow, Heat Transfer and Boiling in Micro-Channels. Springer Press.

Yun, R., Kim, Y., 2004a. Two-phase pressure drop of CO_2 in mini tubes and microchannels. Microscale Thermophys. Eng. 8, 259–270.

Yun, R., Kim, Y., 2004b. Flow regimes for horizontal two-phase flow of CO_2 in a heated narrow rectangular channel. Int. J. Multiphase Flow 30, 1259–1270.

Yun, R., Kim, Y., Kim, M.S., 2005a. Convective boiling heat transfer characteristics of CO_2 in microchannels. Int. J. Heat Mass Transfer 48, 235–242.

Yun, R., Kim, Y., Kim, M.S., 2005b. Flow boiling heat transfer of carbon dioxide in horizontal mini tubes. Int. J. Heat Fluid Flow 26, 801–809.